VISER

Research Article **Open Access**

Toward High Capacity and Stable SnO₂ Hollow Nanosphere Electrode Materials: A Case Study of Ni-substituted Modification

Yannan ZHANG [1], Peng DONG [1], Yingjie ZHANG [1], Hong GUO [2*]

1 National and Local Joint Engineering Laboratory for Lithium-ion Batteries and Materials Preparation Technology, Yunnan Provincial Laboratory for Advanced Materials and Batteries Application, Faculty of Metallurgical and Energy Engineering, Kunming University of Science and Technology, Kunming 650093, Yunnan, PR China
2 School of Materials and Energy, Yunnan Key Laboratory for Micro/Nano Materials and Technology, Yunnan University, Kunming 650091, China

*Corresponding Author: Hong GUO, No. 2, Green Lake North Road, Kunming 650091, China; guohong@ynu.edu.cn (H. Guo)

Abstract:

To develop the urgent requirement for high-rate electrodes in next-generation lithium-ion batteries, SnO₂-based negative materials have been spotlighted as potential alternatives. However, the intrinsic problems, such as conspicuous volume variation and unremarkable conductivity, make the rate capability behave badly at a high-current density. Here, to solve these issues, this work demonstrate a new and facile strategy for synergistically enhancing their cyclic stability by combining the advantages of Ni doping and the fabrication of hollow nanosphere. Specifically, the incorporation of Ni²⁺ ions into the tetragonal rutile-type SnO₂ shells improves the charge transfer kinetics effectively, leading to an excellent cycling stability. In addition, the growth of surface grains on the hollow nanospheres are restrained after Ni doping, which also reduces the unexpected polarization of negative electrodes. As a result, the as-prepared Ni doped electrode delivers a remarkable reversible capacity of 712 mAh g⁻¹ at 0.1 A g⁻¹ and exhibits outstanding capacity of 340 mAh g⁻¹ at 1.6 A g⁻¹, about 2.58 times higher than that of the pure SnO₂ hollow sample.

Keywords: Tin oxide; Negative materials; Nickel doping; Hollow nanospheres; Lithium ion batteries

1 Introduction

Lithium-ion batteries (LIBs) have attracted considerable attention as wide applications in smart grids devices, portable devices and hybrid electric vehicles [1-3]. However, the commercial graphite negative electrodes used at present exhibit a poor theoretical specific capacity (372 mA h g⁻¹) and limited rate capability [4-6]. Therefore, it is important to explore other negative electrodes with high mass energy density. As promising negative electrode candidate for contemporary LIBs, tin dioxide (SnO₂) has attracted huge amount of interest because of its remarkable theoretical capacity (1492 mAh g⁻¹), nontoxicity, abundant tin resource, and favorable processability. Unfortunately, the SnO₂ based LIBs are restricted by huge volume expansion (approximately 240%) during lithiation/delithiation process, leading to agglomeration, structure collapse and finally electrochemical inactivation for the active material [7-10]. In addition, the low electrical conductivity also limits the extensive commercial application of the tin-based LIBs [11-13].

In order to overcome the poor durability and enhance the long-term cycling stability, SnO₂-based materials with special nanostructures are designed and synthesized, such as core-shell particles[14-15], nanotubes[16-20], and nanosheets [21-23]. Among them, porous hollow nanospheres have attracted much attention since they can provide much more cushion space during the lithiation/delithiation process and deliver better cycling stability than other nanostructured materials [24-27].

The electrochemical performance of SnO₂ hollow nanospheres could be further enhanced by elevating their electrical conductivity. One of the most commonly reported strategies is to combine the nano-scaled SnO₂ with conductive carbonaceous materials [28-30]. Another effective approach is to enhance the intrinsic conductivity through introducing transition metal dopant into the SnO₂ structure, the substitution of Sn by cations, such as Sb⁵⁺, Co³⁺, Fe³⁺and Mo⁶⁺can also stabilize the structure of SnO₂ and restrain the tremendous initial capacity loss [31-33]. Ma et al. prepared Co-doped nanoparticles, which exhibited a favorable specific capacity of 493 mAh g⁻¹ under 100 mA g⁻¹ after 50 cycles, almost the 2 times than the undoped one [34]. Zhao et al. synthesized Pd-doped graphene SnO₂

nanocomposite through electroless plating method, the as-prepared SnO_2 nanoparticles delivered high reversible capacity and promising rate capability [35].

Hence, the doping cations properties play an important role in determining the comprehensive performance of the SnO_2, especially for processes of nanostructure, grain growth and internal Li-ion transport in the tetragonal rutile structure. Understanding these effects is important. To the best of our knowledge, Ni^{2+} and Sn^{4+} have the same radius (0.069 nm), Ni^{2+} ions are easily introduced into the SnO_2 lattice. Herein, by combining the strengths of hollow nanostructure and doping element, we report a comparative investigation of pure SnO_2 hollow nanospheres and a series of Ni-doped SnO_2 (NTO) with different dopant contents, focusing on the influence of the dopant concentration on the nanostructure, surface chemical properties as well as electrochemical performance. The results reveal that the Ni^{2+} dopant ratio not only affects the surface chemical properties, but moreover also plays an important role on the electrochemical performance.

2 Experimental

2.1 Material Synthesis

The Ni-doped SnO_2 (NTO) hollow spheres were prepared by following a combined template process and sol-gel process: (1) SiO_2 nanospheres were synthesized by the well-known Stöber method, which was reported in our previous work [36]. (2) 3 g $SnCl_2 \cdot 2H_2O$ was added into a flat bottom boiling flask and then heated to 80℃, after that, the obtained molten $SnCl_2$ and 2 g SiO_2 nanospheres (prepared in the previous step) were dispersed in 200 mL deionized water by ultrasound for 50 min, and the resulting gel was continuously stirred for 36 h at 80℃. (3) Subsequently, several groups with different proportions of $NiSO_4$ were added into the mixture, the Sn: Ni molar ratio used is 40:0, 40:1, 40:2, and 40:3, respectively. (4) Then, the resulting gel was continuously stirred for 36 h at 80℃ to enable the infiltration of tin precursor into the pores of the SiO_2 nanospheres. (5) Ultimately, the four collected products were calcinated at 500℃ for 6 h under an nitrogen flow, and then etched by an HF solution (10%, 100 mL), the four group of Ni-doped SnO_2 (NTO) samples with different dopant contents were obtained (denoted as NTO-0, NTO-1, NTO-2, and NTO-3). The flowchart for the preparation of NTO hollow nanospheres is shown in Figure 1.
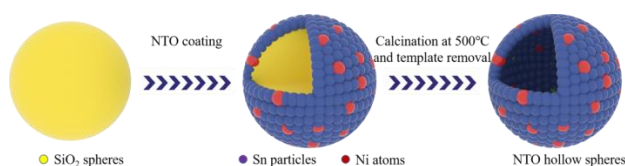

Figure 1 Flowchart for the preparation of nickel doped SnO_2 hollow nanospheres (NTO)

2.2 Material Characterization and electrochemical measurements

The crystalline structure of the as-prepared NTO-x (x=0, 1, 2, and 3) hollow nanospheres were accomplished by X-ray diffraction (XRD, Rint-2000, Japan) using Cu-Kα radiation (1.5412 Å). The surface morphologies and the samples were observed through a field emission scanning electron microscopy (FESEM, Zeiss Supra 55VP), and the elemental distribution was recorded with an energy-dispersive X-ray spectroscopy (EDS, PHI5000 Versa probe-II). The determination of surface elements of the as-prepared powers was carried out by an X-ray photoelectron spectroscopy (XPS, PHI5000 Versaprobe-II). The crystalline microstructures of the obtained powers were further confirmed by the transmission electron microscopy (TEM, FEI Tecnai F20). The electrochemical properties of the as-prepared four samples were further evaluated using CR2025-type coin cells with a multi-channel current static system (LAND CT2001D, China). In addition, the cyclic voltammetry (CV) and the electrochemical impedance spectroscopy (EIS) results of the electrodes were recorded on an electrochemical workstation (PGSTAT302N, Switzerland). The button battery assembly process and the detailed electrochemical analysis procedures were performed according to our previous report [37-38].

3 Results and Discussion

Figure 2a plots the XRD patterns of the four different nickel doped as-prepared NTO samples. Noticeably, All of the NTO samples are well crystallized. The diffraction peaks of four samples can be identified as tetragonal rutile SnO_2 (JCPDS card No. 41-1445) [39-40], and no obvious other impurities are detected, revealing that the Ni^{2+} are favorably integrated with the surface of the SnO_2 shells, and may diffuse only a few nanometers into the tetragonal rutile structure during high temperature post calcination. The magnified diffraction peaks of (110) are exhibited in Figure 2b, it can be clearly observed that the position shifts to a positive degree and the diffraction peaks of (110) deliver a wider half-peak width after Ni-doping. According to Scherer's formula, the thickness of single grain (d) is inversely proportional to half of peak width (B), which reveals that the average lattice parameter is decreased after Ni-doping. The initial particle size of NTO-1、NTO-2、NTO-3 are 9.3 nm 8.6 nm，7.5 nm，and 7.1 nm respectively. This is because even though Ni^{2+} and Sn^{4+} have the same radius (0.069 nm), the incorporation of Ni^{2+} into the lattice of SnO_2 will produce some new defects such as dislocations and vacancies, and the vacancy formation energy and the surface energy of SnO_2 nano-particles are also increased, which can effectively restrain the growth of the crystal to some extent. This phenomenon is further confirmed by the TEM images and in very good agreement with the previous studies on Fe/Zn/Co-doped tin oxide[41-44].
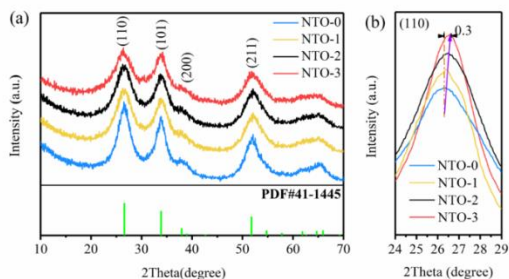
Figure 2 XRD patterns of NTO powder samples (a) and the enlarged (110) peaks (b)

The chemical compositions of the as-prepared hollow nanospheres were further explored by XPS analysis. The full-scan spectra of NTO-0 and NTO-2 samples are exhibited in Figure 2a. Compared with the NTO-0, besides the Sn 3d, O 1s, and C 1s peaks, a couple of weak peaks of Sn 2p can be observed in the spectra of NTO-2 sample. Figure 3b plots the Sn3d spectra of sample NTO-0 and sample NTO-2. The two remarkable shake-up peaks located at 485.6 and 494.4 eV can be assigned to Sn $3d_{5/2}$ and Sn $3d_{3/2}$ levels, respectively[45-46]. A positive shift with approximately 0.4 eV in the sample of NTO-2 indicates the multi-electrons may have transferred from Sn to the doped Ni. Furthermore, the Ni 2p spectra of NTO-2 is illustrated in Figure 3c. Two characteristic peaks at approximately 854.8 eV and 873.2 eV are attribute to Ni $2p_{3/2}$ and Ni $2p_{1/2}$ levels, and two shake-up satellites are located at 861.8 eV and 880.1 eV, respectively, which are attribute to the multi-electron transitions. The binding energy between these characteristic peaks is approximately 18.4 eV. The results show that the nickel element doped into the crystal lattice of SnO_2 exists in the form of Ni^{2+} ions [47-48].
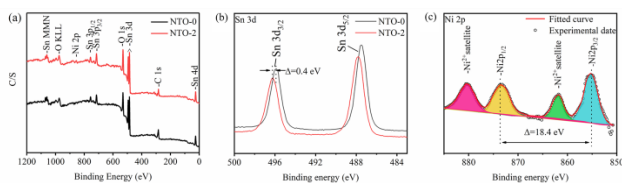
**Figure 3** XPS spectra of NTO-0 and NTO-2 sample: (a) Survey spectrum, (b) Sn 3d5/2, (c) Ni 2p

The morphology and particle size of as-synthesized SiO_2 nanoparticles was investigated by scanning electron microscopy (SEM). As shown in Figure 4a. The obtained SiO_2 exhibits a regular spherical structure with an average diameter of 500-580 nm. Figure 4b displays the SEM images of NTO samples with different Ni doping content, and the magnified image of NTO-2 sample is displayed in Figure 4c, clearly revealing that the presence of a hollow structure for the as-prepared materials. The diameter of SnO_2 spheres with different doping content possess similar values of approximately 550 nm, which in consistent with the size of nano SiO_2 templates. The elemental distribution of the as-prepared NTO-2 sample

was further detected by EDS test (Figure 4d). The uniform distributions of Sn, O, and Ni elements over the whole hollow spheres indicates that the Ni is homogeneously and continuously coupled with the SnO_2 shells.
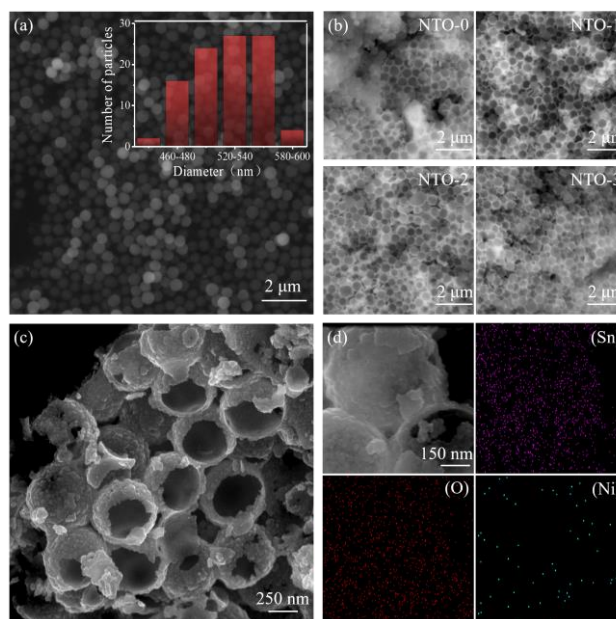

Figure 4 SEM images of (a) SiO_2 nanoparticles; (b) SEM image of NTO samples with different Ni doping content; (c) magnified image of NTO-2;(d) EDS mapping images of NTO-2

TEM images of as-prepared products are displayed in Figure 5. The spherical morphology of SiO_2 exhibits regular and clear surface profiles, as shown in Figure 5a. The TEM images in Figure 5 (b-f) were captured to further confirm that the as-synthesized SnO_2 samples exhibit hollow nanosphere structures. It can be clearly seen that spherical morphology of $SnO_2@SiO_2$ can be well maintained after etching of the SiO_2 exhibits a shell thickness of approximately 42 nm (Figure 5b). However, after Ni doping, the shell thickness of the NTO-2 sample is decreased to approximately 28 nm through the same process (Figure 5c). Furthermore, Figure 5d-e clearly exhibit the high-resolution TEM (HRTEM) images of the lattice fringes and particle size of the two samples. The grain diameters of NTO-0 and NTO-2 are approximately 5-7 nm and 8-9 nm, respectively, which coincides well with the previous XRD calculation results. This is because the crystallization and ripening process of the SnO_2 primary particle particles may be effectively restrained by the sequential accumulation of Ni^{2+}, which is similar to the process of the crystal surface energy model. The selected-area electron diffraction (SAED) pattern of NTO-2 with the diffraction rings from inside to outside can be indexed to (110), (101), (200), (211), and (311) of tetragonal rutile SnO_2, as illustrated in Figure 5f [49]. This result reveals that expect for the suppression of the particles growth, the Ni doping does not cause any changes in the tetragonal rutile structure of SnO_2.
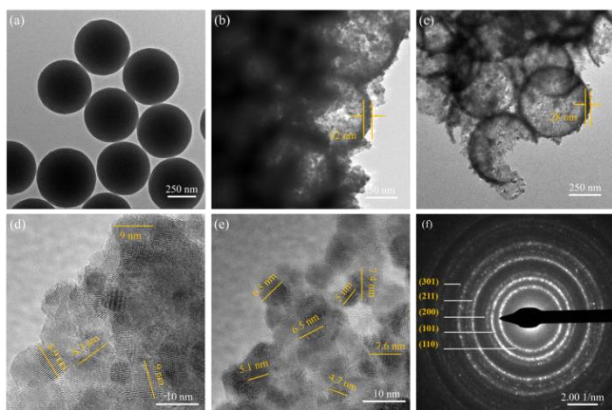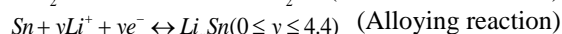
Figure 5 TEM images (a) SiO₂ nanoparticles, (b) NTO-0, and (c) NTO-2, respectively；high-resolution TEM image of (d) NTO-0, and (e) NTO-0；(d) the selected-area electron diffraction (SAED) pattern of NTO-2 sample
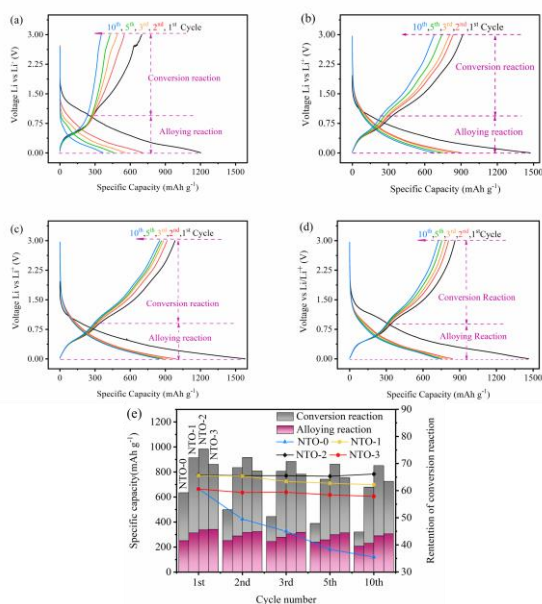
Figure 6 The charge-discharge test curves of the NTO negative electrodes: (a) NTO-0; (b) NTO-1; (c) NTO-2；(d) NTO-3; (e) the relationship between capacity retention for the conversion reaction and the total specific charge capacities of all the samples

Figure 6a-d display the charge-discharge curves of the prepared four NTO samples at a current density of 100 mA g⁻¹ between 0.01 V and 3.0 V. The initial discharge and charge-specific capacities of the NTO-0, NTO-1, NTO-2, and NTO-3 samples are1203 mAh g⁻¹、1470 mAh g⁻¹、1581 mAh g⁻¹, and 1463 mAh g⁻¹, and the initial coulombic efficiency of these sample are 61.6%，62.0%，62.5%, and 58.8%, respectively. All the samples suffer serious capacity losses in the early cycles, which is attribute mainly to the SEI film formation and the production of Li₂O [35]. NTO-2 exhibits the best charge-specific capacity of 850 mAh g⁻¹ after 10th cycles even with a rather moderate initial coulombic efficiency,

which is almost twice of the undoped NTO-0 sample (466 mAh g⁻¹). Figure 6e shows the relationship between capacity retention for conversion reaction and the total specific charge capacities of the four samples. It can be clearly seen that the capacity ratio of the conversion reaction of Ni doped samples are significantly higher than that of the undoped one. After the 10th cycles, the capacity ratio of conversion reaction for the NTO-0 sample is only 35.5%, while the capacity ratio of the NTO-2 is increased up to 66.1%. Thus, we conclude that the Ni doping could facilitate the conversion reaction between Sn and Li₂O, which results in the remarkable conversion reaction capacity [50].

$$SnO_2 + 4Li^+ + 4e^- \rightarrow Sn + 2Li_2O \quad \text{(Conversion reaction)}$$
$$Sn + yLi^+ + ye^- \leftrightarrow Li_ySn (0 \le y \le 4.4) \quad \text{(Alloying reaction)}$$

To evaluate the cycling performance of NTO hollow sphere with different Ni doping content, a range of cyclic tests were carried out at the current density of 100 mA g⁻¹ in the voltage range of 0.01-3.0V, as presented in Figure 7a. After 100 cycles, the capacity of the NTO-0 decays rapidly to 236 mAh g⁻¹ with a deteriorating capacity retention of 32.0%, whereas the NTO can still maintain promising capacity retention of 73.1% (712 mAh g⁻¹) with a nearly perfect coulombic efficiency (approximately 100%), except during the first cycle. In addition, the NTO-1 and NTO-3 also can deliver the moderate charge capacity of 485 and 653 mAh g⁻¹. Based on these results, we conclude that the electrochemical performance of the SnO₂ nano hollow spheres are improved by the Ni doping.

Furthermore, the rate capabilities of these four samples were also investigated by applying different specific currents, i.e., 0.05, 0.1, 0.2, 0.4, 0.8, and 1.6 A g⁻¹, as shown in Figure 7b. As increasing the current density, compared with the sample NTO-0, all of the samples deliver significantly improved charge capacities after doping under each current density (0.05-1.6 A g⁻¹). Notably, sample NTO-2 exhibits the best rate performance, its charge capacity can remain up to 340 mAh g⁻¹even at 1.6 A g⁻¹ current density, and exhibit a promising charge capacity of 651 mAh g⁻¹ when the current density is recovered to 0.1 Ag⁻¹, whereas the pristine sample NTO-0 deliver the limited rate performance. The results of the cyclic and rate performances are consistent with our previous corresponding charge and discharge profiles.
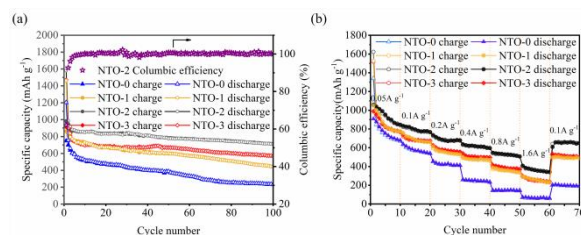
Figure 7 (a) Cycling performance of NTO samples at a current density of 100 mA g⁻¹; (b) rate performance of NTO samples.

For better understanding the kinetic process of lithium insertion/extraction into/from the 3D Ni doped SnO_2 hollow spheres, cyclic voltammetry (CV) tests between 0.01-3.0 V at different scanning rates (0.1-0.8 mV s^{-1}) were performed for the samples NTO-0 and NTO-2. Two characteristic pairs of redox peaks can be clearly observed in Figure 8a. The first pair located at 0.10 and 0.82 V (a site) are ascribed to the of Li_xSn (0 < x < 4.4) alloying and de-alloying process. The second dominant anodic peak located at 1.58 V (c site) is related to the partial conversion of Sn to Sn^{4+}, while the cathodic peak observed at 1.13 V is attributed to the irreversible formation of a SEI film and the reduction reaction of SnO_2 by Li. NTO-0 exhibits a large peak shift and obvious polarization at different scanning rates.

For the sample of NTO-2, the shape of the CV profiles (Figure 8b) is similar to that of the NTO-0 sample. It is worthy to note that the initial anodic peaks shift to 0.8 and 1.54 V, respectively. The redox potential difference related to the Li_xSn alloying/de-alloying process is lower than that of the undoped one. Moreover, the peak displacement of sample NTO-2 is decreased, and the cyclic voltammetry profiles remain unchanged as the increase of the scanning rate, revealing the reduced polarization and improved reversibility.

The Li^+ diffusion coefficient change of electrodes can be obtained from Randles-Sevcik equation (1):

$$I_p = 2.69 \times 10^5 n^{3/2} A D^{1/2} v^{1/2} C_0 \tag{1}$$

in which D, I_p, n, A, v, and C_0 represents the diffusion coefficient of Li^+, the oxidation peak current (a and c site in Figure 9a-b), the amount of electrons transferred per SnO_2 molecule in the electrochemical reaction, the area of the electrode, scanning rate, and the concentration of Li^+. Since the area, charge transfer number, and the Li^+ concentration of the two samples are approximately identical, the ratio of the Li^+ diffusion coefficient between the two sample is proportional to the value of $(I_p/v^{1/2})^2$, as shown in Figure 8c. Consequently, the D_{NTO-2}/D_{NTO-0} at a and c site are 1.31 and 1.33, respectively, indicating that Ni^{2+} doping can effectively enhance the Li^+ diffusion.
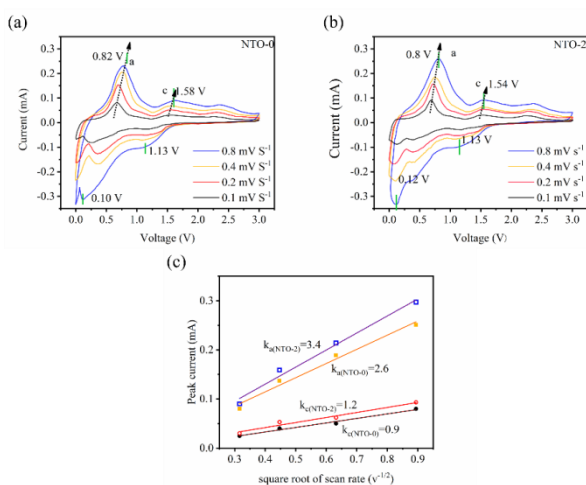
To further explore the beneficial effect of Ni doping on the electrochemical properties, electrochemical impedance spectroscopy (EIS) measurements were conducted to analyze the reaction dynamics. The Nyquist plots of four NTO samples after 5 cycles are shown in Figure 9. The semicircles in the high and high-middle frequency regions represent the solid electrolyte interface (SEI) resistance (Rf) and the charge transfer resistance (R_{ct}), whereas the inclined line in the low-frequency region corresponds to the Warburg impedance (Z_w) [51-52]. The diameter of the semicircle corresponding to the three doped sample are obviously smaller than that of the pristine one. Notably, the calculated he SEI resistance (R_f) of NTO-2 is 5.1Ω, which is lower than that of the NTO-0 (7.2 Ω), revealing that Ni doping can alleviate the thickness increase of the solid electrolyte interface membrane. The charge-transfer resistance (R_{ct}) of NTO-2 is simulated as 51.2 Ω, which is obviously lower than that of the NTO-0 (129.5Ω), indicating the charge transfer efficiency of SnO_2 hollow spheres is significantly improved. The favorable reversible specific capacity, enhanced cycling stability and remarkable rate capability of the NTO-2 sample could be attributed to the following two factors:(1) A certain amount of Ni^{2+} incorporates with SnO_2 can not change the integrity of the original tetragonal rutile structure but change the kinetics of SnO_2 negative materials, the charge transfer impedance is significantly decreased, resulting in the accelerated charge transfer kinetics. (2) The crystallization and ripening process of the primary particles is restrained by the Ni doping, and the shell thickness is also reduced, which effectively facilitate the Li^+ diffusion and internal electron transport in the active materials.
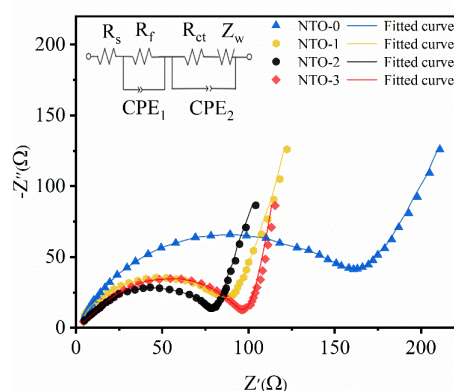
Figure 9 The Nyquist plots of the NTO samples

4 Conclusion

In summary, the SnO_2 hollow nanospheres with three different nickel dopant ratios were successfully synthesized through combined the template with the hydrothermal strategies and applied in LIBs as a negative material. XPS profiling with EDS mapping results reveal that the nickel dopant is uniformly distributed and well

Figure 8 Cyclic voltammograms curves of NTO-0 (a), NTO-2 (b) at different scanning rates; (c) anodic peak against root of scan rate for NTO-0 and NTO-2

incorporated into SnO_2 shells among the hollow materials. The dopant concentration does not only have an influence on the on the surface chemistry property, but moreover on the electrochemical performance. Electrochemical measurement results indicate that the electrodes doped with 5% (wt%) can deliver an outstanding rate performance and excellent cycling performance (exhibit a favourable reversible capacity of 712 mAh g^{-1} at 100 mA g^{-1} after 100 cycles and deliver 340 mAh g^{-1} at 1.6 A g^{-1}). Without carbon coating, this hollow structural fabrication combined with rational dopant ratios will illuminate the path for developing other negative materials for solving the problems of low rate capability and poor cyclic stability.

References

[1] Ma D, Li Y, Mi H, et al., Robust SnO_{2-x} nanoparticle-impregnated carbon nanofibers with outstanding electrochemical performance for advanced sodium-ion batteries, Angew. Chem. Int. Ed. 57 (2018): 8901-8905.

[2] Tan L, Feng S.H, Li X H, et al., Oxygen-induced lithiophilicity of tin-based framework toward highly stable lithium metal anode. Chem. Eng. J. 394 (2020): 124848.

[3] N. Mahmood, Tang T Y, Hou Y L. Nanostructured anode materials for lithium ion batteries: progress, challenge and perspective, Adv. Energy Mater. 6 (2016): 1600374.

[4] Wang L, Y. Leconte, Feng Z, et al., Novel preparation of N-doped SnO_2 nanoparticles via laser-assisted pyrolysis: demonstration of exceptional lithium storage properties. Adv. Mater. 29 (2017): 1603286

[5] V.M.H. Ng, Wu S Y, Liu P J, et al., Hierarchical SnO_2-graphite nanocomposite anode for lithium-ion batteries through high energy mechanical activation, Electrochim. Acta 248 (2017): 440-448.

[6] Zhang F, Yang C K, Gao X, et al., SnO_2@PANI core–shell nanorod arrays on 3D graphite foam: a high-performance integrated electrode for lithium-ion batteries, ACS Appl. Mater. Interfaces 9 (2017): 9620-9629.

[7] Tian Q, Zhang F, Yang L. Fabricating thin two-dimensional hollow tin dioxide/carbon nanocomposite for high-performance lithium-ion battery anode. Appl. Surf. Sci. 481 (2019): 1377-1384.

[8] Shi S.J, Deng T T, Zhang M, et al., Fast facile synthesis of SnO_2/graphene composite assisted by microwave as anode material for lithium-ion batteries, Electrochim. Acta 246 (2017): 1104-1111.

[9] Zhang L, Jiang L, Yan H, et al., Mono dispersed SnO_2 nanoparticles on both sides of single layer graphene sheets as anode materials in Li-ion batteries. J. Mater. Chem. 20 (2010): 5462-5467.

[10] Lou X, Deng D, Lee J, et al., Preparation of SnO_2/carbon composite hollow spheres and their lithium storage properties. Chem. Mater. 20 (2008): 6562-6566.

[11] Zhu Z, Wang S, Du J, et al., Ultrasmall Sn nanoparticles embedded in nitrogen-doped porous carbon as high-performance anode for lithium-ion batteries, Nano Lett. 14 (2014): 153-157.

[12] Yi L G, Liu L, Guo G X, et al., Expanded graphite@SnO_2@polyaniline composite with enhanced performance as anode materials for lithium ion batteries, Electrochim. Acta 240 (2017): 63-71.

[13] Hou C C, S. Brahma, Weng S C, et al., low temperature synthesis of SnO_2/reduced graphene oxide nanocomposite as anode material for lithium-ion batteries, Appl. Surf. Sci. 413 (2017): 160-168.

[14] Zhu Z, Wang S, Du J, et al., Ultrasmall Sn nanoparticles embedded in nitrogen-doped porous carbon as high-performance anode for lithium-ion batteries, Nano Lett. 14 (2014): 153-157.

[15] Hong Y, Mao W, Hu Q, et al., Ai, Nitrogen-doped carbon coated SnO2 nanoparticles embedded in a hierarchical porous carbon dramework for high-performance lithium-ion battery anodes, J. Power Sources 428 (2019): 44-52.

[16] Zhou X, Yu L, Lou X W D. Formation of uniform N-doped carbon-coated SnO_2 submicroboxes with enhanced lithium storage properties, Adv. Energy Mater. 6 (2016): 1066451.

[17] Zhang L, Wu H B, Liu B, et al., Formation of porous SnO_2 microboxes via selective leaching for highly reversible lithium storage, Energy Environ. Sci. 7 (2014): 1013-1017.

[18] Huang B, Li X, Pei Y, et al., Novel carbon-encapsulated porous SnO_2 anode for lithium-ion batteries with much improved cyclic stability, Small 12 (2016): 1945-1955.

[19] D. Kim, D. Lee, J. Kim, et al. Electrospun Ni-added SnO_2-carbon nanofiber composite anode for high-performance lithium-ion batteries, ACS Appl. Mater. Interfaces 4 (2012): 5408-5415.

[20] Li H Z, Yang L Y, Liu J, et al., Improved electrochemical performance of yolk-shell structured SnO_2@void@C porous nanowires as anode for lithium and sodium batteries, J. Power Sources 324 (2016): 780-787.

[21] Chang L, Yi Z, Wang Z, et al., Ultrathin SnO2 nanosheets anchored on graphene with improved electrochemical kinetics for reversible lithium and sodium storage, Appl. Surf. Sci. 484 (2019): 646-654.

[22] Ding S, Luan D, F Boey, SnO_2 nanosheets grown on graphene sheets with enhanced lithium storage properties, Chem. Commun. 47 (2011): 7155-7157.

[23] Wei W, Du P, Liu D, et al., Facile mass production of nanoporous SnO_2 nanosheets as anode materials for high performance lithium-ion batteries, J Colloid Interf. Sci. 503 (2017): 205-213.

[24] Luo G E, Liu W J, Zeng S S, et al., Hierarchal mesoporous SnO_2@C@TiO_2 nanochains for anode material of lithium-ion batteries with excellent cycling stability, Electrochim. Acta 184 (2015): 219-225.

[25] Wu P, Du N, Zhang H, et al., Self-templating synthesis of SnO_2-carbon hybrid hollow spheres for superior reversible lithium ion storage, ACS Appl. Mater. Interfaces 3 (2011): 1946-1952.

[26] Hong Y J, Son M Y, Kang Y C. One-pot facile synthesis of

double-shelled $SnO_{(2)}$ yolk-shell-structured powders by continuous process as anode materials for Li-ion batteries, Adv. Mater. 25 (2013): 2279-2283, 2250.

[27] Ma D Q, Dou P, Yu X H, et al., Novel hollow SnO_2 nanosphere@TiO_2 yolk–shell hierarchical nanospheres as anode material for high-performance lithium-ion batteries, Mater. Lett. 157 (2015): 228-230.

[28] Yi L G, Liu L, Guo G X, et al., Expanded graphite@SnO_2@polyaniline composite with enhanced performance as anode materials for lithium ion batteries, Electrochim. Acta 240 (2017): 63-71.

[29] Hu L L, Yang L P, Zhang D, et al., Designed synthesis of SnO_2-C hollow microspheres as an anode material for lithium-ion batteries, Chem. Commun. 53 (2017): 11189-11192.

[30] Liu Q, Dou Y, Ruan B, et al., Carbon-Coated Hierarchical SnO_2 hollow spheres for lithium ion batteries, Chem. Eur. J. 22 (2016): 5853-5857.

[31] Wang Y, I. Djerdj, B. Smarsly, et al., Antimony-doped SnO_2 nanopowders with high crystallinity for lithium-ion battery electrode, Chem.Mater. 2009, 21: 3202-3209.

[32] Yan Y, Du F, Shen X, et al., Large-scale facile synthesis of Fe-doped SnO_2 porous hierarchical nanostructures and their enhanced lithium storage properties. J. Mater. Chem. A 2 (2014): 15875-15882.

[33] Wang X K, Li Z Q, Zhang Z W, et al., Mo-doped SnO_2 mesoporous hollow structured spheres as anode materials for high-performance lithium ion batteries, J. Mater. Chem. A 2 (2015): 3604-3613.

[34] Ma Y.J, Ma Y, U. Ulissi, et al., Influence of the doping ratio and the carbon coating content on the electrochemical performance of Co-doped SnO_2 for lithium-ion anodes, Electrochim. Acta 277 (2018): 100-109.

[35] Zhao P, Yue W B, Yuan X, et al., Exceptional lithium anodic performance of Pd-doped graphene-based SnO_2 nanocomposite. Electrochim. Acta 225 (2017): 322-329.

[36] W. Stöber, A. Fink, E. Bohn, Controlled growth of monodisperse silica spheres in the micron size range, J. Colloid and Interf. Sci. 26 (1968): 62-69.

[37] Wang S, Yu X H, Liu J X, et al., Encapsulation of SnO_2 nanoparticles between the hollow TiO_2 nanosphere and the carbon layer as high-performance negative materials for lithium-ion batteries, J. Alloy. Compd. 814 (2020): 152342-152349.

[38] Zhang Y N, Zhang J J, Rong J, et al., Design and controllable synthesis of core-shell nanostructured Ni-P particles with an ionothermal strategy, J. Alloy. Compd. 795 (2019): 177-186.

[39] Wang Y, Guo W B, Yang Y Q, et al., Rational design of SnO_2@C@MnO_2 hierarchical hollow hybrid nanospheres for a Li-ion battery anode with enhanced performances, Electrochim. Acta 262 (2018): 1-8.

[40] Cui D M, Zheng Z, Peng X, et al., Fluorine-doped SnO_2 nanoparticles anchored on reduced graphene oxide as a high-performance lithium ion battery anode, J. Power Sources 362 (2017): 20-26.

[41] F. Mueller, A. Gutsche, H. Nirschl, et al., Iron-doped ZnO for lithium-ion anodes: impact of the dopant ratio and carbon coating content, J. Electrochem. Soc. 164 (2017): A6123-A6130.

[42] F. Mueller, D. Bresser, V.S.K. Chakravadhanula, S. Passerini, Fe-doped SnO_2 nanoparticles as new high capacity anode material for secondary lithium-ion batteries, J. Power Sources 299 (2015): 398-402,

[43] P. Nithyadharseni, K.P. Abhilash, S. Petnikota, et al., Synthesis and lithium storage properties of Zn, Co and Mg doped SnO_2 nano materials, Electrochim. Acta 247 (2017): 358-370,

[44] D. Bresser, F. Mueller, M. Fiedler, et al., Transition-metal-doped zinc oxide nanoparticles as a new lithium-ion anode material, Chem. Mater. 25 (2013): 4977-4985.

[45] J.Y. Cheong, C. Kim, J.-W. Jung, et al., Incorporation of amorphous TiO_2 into one-dimensional SnO_2 nanostructures as superior anodes for lithium-ion batteries, J. Power Sources 400 (2018): 485-492.

[46] Pan L, Zhang Y, Lu F, et al., Exposed facet engineering design of graphene-SnO_2 nanorods for ultra-stable Li-ion batteries, Energy Storage Mater. 19 (2019): 39-47.

[47] T.I. Koranyi, Z. Vit, D.G. Po et al.duval, R. Ryoo, H.S. Kim, E.J.M. Hensen, SBA-15-supported nickel phosphide hydrotreating catalysts, J. Catal. 253 (2008): 119-131.

[48] Y. Okamoto, Y. Nitta, T. Imanaka, et al., Surface characterisation of nickel boride and nickel phosphide catalysts by X-ray photoelectron spectroscopy, J. Chem. Soc. 75 (1979): 2027-2039.

[49] Zhu C R, Xia X H, Liu J L, et al., TiO_2 nanotube@SnO_2 nanoflake core–branch arrays for lithium-ion battery anode, Nano Energy 4 (2014): 105-112.

[50] Cheng Y Y, Huang J F, Qi H, et al., Adjusting the chemical bonding of SnO_2@CNT composite for enhanced conversion reaction kinetics, Small 13 (2017): 1700656.

[51] Wang X L, Li J Z, Chen Z, et al., Hierarchically structured C@SnO_2@C nanofiber bundles with high stability and effective ambipolar diffusion kinetics for high-performance Li-ion batteries, J. Mater. Chem. A 4 (2016): 18783-18791.

[52] Wang H M, Yan Y, Chen G. The effects of confinement on TiO_2@SnO_2@TiO_2 hollow spheres for high reversible lithium storage capacity, J. Alloy. Compd. 778 (2019): 375-381.